



Modeling the long-term fate of injected CO₂ in saline aquifers: An integrated framework coupling multiphase flow, dissolution, reaction, and ripening

Ruiqi Chen¹, Wenjie Xu^{2,3,*}, Yunmin Chen^{2,3}, Qingping Li¹, Tianyuan Zheng^{4,*} and Bo Guo⁵

¹Beijing Huairou Laboratory, Beijing 101499, China

²Center for Hypergravity Experimental and Interdisciplinary Research, Zhejiang University, Hangzhou 310058, China

³MOE Key Laboratory of Soft Soils and Geoenvironmental Engineering, Zhejiang University, Hangzhou 310058, China

⁴College of Environmental Science and Engineering, Ocean University of China, Qingdao 266100, China

⁵Department of Hydrology and Atmospheric Sciences, University of Arizona, 85719 Tucson, AZ, United States

Correspondence to: Wenjie Xu (wenjiexu@zju.edu.cn) & Tianyuan Zheng (zhengtianyuan@ouc.edu.cn)

Abstract. Geological carbon sequestration (GCS) mitigates climate change by storing anthropogenic carbon dioxide (CO₂) in geological formations. CO₂ undergoes complex physical and chemical transformations in the deep geological formations, governed by various interacting trapping mechanisms. Because the trapping mechanisms operate at wide range of different timescales, their long-term interplay remains unclear. We develop an integrated numerical modeling framework to analyze and track the footprint and phase transition processes that occur throughout the entire cycle of the injected CO₂ in saline aquifers. The key novelty of the modeling framework lies in its capability to accurately describe multiple hydrodynamic processes and their interactions, including injection, dissolution-driven convection, reactive transport, and gravity-induced Ostwald ripening. The results suggest that dissolution reduces the lateral migration of physically trapped CO₂, while mineral reaction provides a preferential channel for CO₂-rich flow. For the scenarios we analyze, after several hundred years of mass transfer, dissolved CO₂ accounts for approximately 40% of total trapping amount, while mineral trapping contributes less than 1%. The results also illustrate that low vertical permeability is unfavorable for the long-term transition of CO₂ from the physical state to the dissolution state. When the heterogeneity index γ increases from 0.5 to 10, the total dissolution storage amount within the domain is reduced to one-third over the 500-year simulation period. This integrated modeling framework provides critical insights into the long-term evolution of CO₂ plume migration and phase transition behavior, thereby offering a practical tool to quantitatively assess the long-term fate of the injected CO₂ in saline aquifers.

1 Introduction

Geological carbon storage (GCS) is a promising technology that involves storing the greenhouse gas CO₂ in underground porous rock formations (Lane et al., 2021; Wei et al., 2021). Once CO₂ is injected into the reservoir at the in-situ pressure and temperature, four trapping mechanisms occur sequentially at varying time scales (Krevor et al., 2023). Structural trapping is when CO₂ moves



upwards below a low-permeability caprock because of buoyancy. Residual trapping occurs when CO₂ bubbles are trapped in the pore structure of the formation. Dissolution trapping and mineral trapping involve the dissolution of CO₂ into brine to form weak acid H₂CO₃, inducing the dissolution and precipitation of rock minerals (Dai et al., 2020a; De Silva et al., 2015). Understanding the spatiotemporal evolution of trapping mechanisms is crucial for the safety and storage efficiency of GCS projects (Ringrose et al., 2021). However, the complex physical and chemical changes at different stages present challenges in predicting the migration pathways of CO₂ in the reservoir.

Field monitoring and laboratory experiments have provided preliminary insights into the long-term migration behavior of CO₂ in geological reservoirs (Dance & Paterson, 2016; Györe et al., 2017; Jackson & Krevor, 2020; Sathaye et al., 2014; Zhou et al., 2020). During the injection period, CO₂ displaces the native brine within rock pores, characterized by a compact displacement front (Birkholzer et al., 2015). Driven by density differences, the injected CO₂ migrates rapidly upward to the top of the reservoir, where it spreads laterally beneath the low-permeability caprock (Jing et al., 2023). Molecular diffusion allows CO₂ to dissolve into undersaturated brine, increasing fluid density and inducing gravitational instability (Emami-Meybodi et al., 2015; Guo et al., 2021). This instability gives rise to convective mixing, which enhances the downward transport of dissolved CO₂ into deeper regions of the reservoir (Neufeld et al., 2010). The dissolution of CO₂ promotes water–rock interactions, leading to carbon mineralization and thereby improving the security of geological storage (Cui et al., 2018). Acidic conditions facilitate carbonate dissolution, which alters the permeability and porosity of the reservoir rock and can generate dissolution features such as wormholes (Sabo & Beckingham, 2021; Seyyedi et al., 2020). Subsequent changes in pore structure further influence the migration pathways of the CO₂ plume. Additionally, under gravitational effects, Ostwald ripening can lead to the secondary redistribution of residual trapped CO₂ bubbles (Xu et al., 2019a).

Numerical modeling of geological carbon storage (GCS) involves a broad spectrum of temporal scales, ranging from injection period lasting several decades to mineral trapping processes that may extend over tens of thousands of years. Moreover, accurately capturing CO₂ migration pathways necessitates the precise representation of meter-scale convective fingering, as well as kilometer-scale macroscopic plume evolution (Elenius et al., 2015). Consequently, developing a numerical model that adequately encompasses the entire life cycle of GCS poses considerable challenges. In recent years, several modeling approaches have been proposed to study GCS over its full duration. Several numerical models have simulated large-scale dissolved CO₂ plume migration, incorporating injection and dissolution processes without considering mineral trapping (Elenius et al., 2015; De Paoli, 2021; Singh et al., 2019). Wang et al. (2022) developed a fully-coupled model that additionally considers drainage and imbibition effects, though geochemical reactions were not included. Reactive transport models based on GCS mainly focus on the long-term transformation of chemical components, with TOUGHREACT being the most typical example (Xu et al., 2011). These reactions significantly alter formation permeability and porosity, thereby influencing fluid flow and solute transport—key factors governing long-term storage efficiency (Fu et al., 2015; Sainz-Garcia et al., 2017a). However, a comprehensive model that integrates multiple long-term trapping mechanisms and captures their mutual interactions remains lacking, largely due to disparities in temporal scales and numerical convergence difficulties.



Based on the above summary, we have, for the first time, developed an integrated numerical model for GCS, coupling the key physical and chemical processes of CO₂ injection, dissolution, convection and reaction. This modeling framework dynamically captures the coupled dynamics of CO₂ transport and phase transition, elucidating the spatiotemporal evolution and complex interactions of various trapping mechanisms over long geological timescales. By explicitly representing these multiscale and multiphase processes within a unified model, our work provides a integrated tool for predicting long-term CO₂ fate and storage security. Finally, we employ the model to systematically investigate the influence of critical factors such as calcite content and reservoir heterogeneity on the long-term fate and transport of CO₂, offering new insights for optimizing storage strategies.

2 Mathematical Description

2.1 Two-phase flow and multicomponent transport

In the saline aquifer system, the mass conservation equation governing two-phase flow in a porous medium can be expressed as follows:

$$\frac{\partial(\phi\rho_w S_w)}{\partial t} - \nabla \cdot \left(\rho_w \mathbf{k} \frac{k_{rw}}{\mu_w} (\nabla p_w - \rho_w \mathbf{g}) \right) = Q_w, \quad (1)$$

$$\frac{\partial(\phi\rho_n S_n)}{\partial t} - \nabla \cdot \left(\rho_n \mathbf{k} \frac{k_{rn}}{\mu_n} (\nabla p_w + \nabla p_c - \rho_n \mathbf{g}) \right) = Q_n, \quad (2)$$

where subscript α (w or n) represents the wetting phase (w, brine) and nonwetting phase (n, CO₂). ϕ denotes the porosity, ρ_α and S_α represents the phase density and saturation. Assuming that only two fluid phases coexist in the pore space, the saturation of the non-wetting phase satisfies $S_n = 1 - S_w$. The intrinsic permeability tensor \mathbf{k} is assumed to be that of a homogeneous and isotropic formation. $k_{r\alpha}$ and μ_α respectively denote the relative permeability and viscosity of phase α , while g represents the gravitational acceleration. The term Q_α refers to the mass source terms arising from geochemical reaction and dissolution processes.

Dissolved carbon dioxide in brine is treated as a solute component. The transport equation for dissolved CO₂, based on Fick's law, is expressed as follows:

$$\frac{\partial(\phi\rho_w S_w X_c)}{\partial t} + \nabla \cdot (\rho_w \mathbf{u}_w X_c - \phi\rho_w S_w D_c \nabla X_c) = Q_w^D + Q_w^C, \quad (3)$$

where X_c represents the mass fraction of CO₂, \mathbf{u}_w is brine velocity and D_c is diffusion coefficient. The source term Q_w^D and Q_w^C represent the dissolution and chemical reaction terms. The dissolved source term Q_w^D is formulated as a function of CO₂ saturation with the mass transfer coefficient κ serving as a key parameter (Martinez & Hesse, 2016). The mechanical dispersion and adsorption of solutes in brine are neglected.

$$Q_w^D = \kappa \phi S_n \rho_w (X_{c,max} - X_c), \quad (4)$$



90 where $X_{c,max}$ is the maximum dissolution mass fraction. Furthermore, the density of brine is assumed to be directly proportional to the local concentration, an approximation commonly referred to as the Boussinesq approximation (Diersch & Kolditz, 2002).

$$\rho_w = \rho_0 + \Delta\rho \frac{X_c}{X_{c,max}}, \quad (5)$$

where ρ_0 is the density of pure brine and $\Delta\rho$ is the density difference between CO₂-saturated and pure brine.

Some studies have shown that the capillary transition zone has a significant impact on the buoyant flow of CO₂ dissolution in saline aquifer (Elenius et al., 2014; Emami-Meybodi & Hassanzadeh, 2015). The capillary pressure is defined as the pressure difference between the non-wetting phase and the wetting phase, $p_c = p_n - p_w$. The capillary pressure–saturation relationship and relative permeability curves of the media are typically described by the Brooks–Corey model. The parameters used are listed in Table 1. Parameter selection refers to reservoir survey data and detailed references.

$$S_w^* = \frac{S_w - S_{wr}}{1 - S_{wr} - S_{nr}}, \quad (6a)$$

100 $p_c = p_{c0} S_w^{*(1/\lambda)}, \quad (6b)$

$$k_{rw} = S_w^{*(2+3\lambda)/\lambda}, \quad (6c)$$

$$k_{rn} = (1 - S_w^*)^2 \left(1 - S_w^* \frac{2+3\lambda}{\lambda} \right), \quad (6d)$$

where S_w^* is normalized wetting phase saturation, S_{wr} and S_{nr} are the residual saturation of the two phases. p_{c0} denotes entry pressure and λ represents pore-size distribution index.

105 **Table 1: Parameters of formation and fluid properties.**

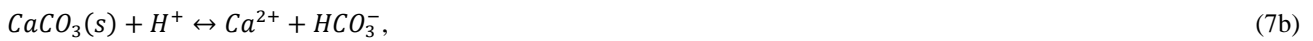
Parameters	Symbols	Values (Unit)
Domain size	$L \times H$	200×50 (m×m) ^a
Porosity	ϕ_0	0.1 (-) ^b
Permeability	k_0	1×10^{-13} (m ²) ^b
Residual saturations	S_{wr}, S_{nr}	0.3, 0.05 (-) ^c
Entry pressure	p_{c0}	10 (kPa) ^d
Pore parameter	λ	2 (-) ^d
Injection rate	r_I	2×10^{-5} (m ³ /s) ^e
Injection time	T_I	100 (d)
Diffusivity coefficient	D_c	2×10^{-9} (m ² /s) ^f
Density of brine and CO ₂	ρ_w, ρ_n	1058, 800 (kg/m ³) ^f
Viscosity of brine and CO ₂	μ_w, μ_n	0.595, 0.0395 (mPa·s) ^f
Maximum dissolution mass fraction	$X_{c,max}$	0.05 (-) ^f
Density increase with CO ₂ dissolution	$\Delta\rho$	10.58 (kg/m ³) ^g
Initial pressure	p_0	20 (MPa) ^d

a (Carrigan et al., 2013) b (Mathias et al., 2013; Saaltink et al., 2013a) c (Iglauer et al., 2011; Pini & Benson, 2013) d (Bennion & Bachu, 2008) e (Kolditz et al., 2012) f (Martinez & Hesse, 2016) g (Ennis-King & Paterson, 2005).



2.2 Geochemical reactions

According to previous studies, calcite have a relatively fast reaction rate among all contents in sandstone (Xu et al., 2019b). The full-cycle model focuses on a relatively short time scale and concentrates on calcium minerals (calcite, dolomite), considering quartz, feldspar, and other minerals as insoluble substances because their dissolution/precipitation process takes thousands of years (De Silva et al., 2015). The formation of carbonate is considered to be the main way to sequester CO₂ and an important process for achieving permanent trapping in GCS (Bachu et al., 1994). To simplify the model, it is assumed that the reservoir minerals involved in the chemical reaction only contain 5% calcite (Sainz-Garcia et al., 2017b). The main geochemical reactions of calcite dissolution in CO₂-rich plume are as follows:



The transport equation for reactive solute transport, accounting for convection, diffusion, and geochemical reactions, can be expressed as follows:

$$\frac{\partial \phi \rho_w S_w X_c}{\partial t} + \nabla \cdot (\rho_w \mathbf{u}_w X_c - \phi \rho_w S_w D_c \nabla X_c) = Q_w^c, \quad (8a)$$

$$Q_w^c = r_c = -k_r a_v c_{CO_2} (c_{CaCO_3})^n, \quad (8b)$$

$$\frac{\partial c_{CaCO_3}}{\partial t} = -k_r a_v c_{CO_2} (c_{CaCO_3})^n, \quad (8c)$$

where r_c is the reaction term of dissolved CO₂, k_r and a_v respectively represent reaction rate constant and mineral surface area available for reaction per volume of the medium. n is the rate of the reaction which is 1 for the second-order reaction. The concentration of component i (CaCO₃ and CO₂) is represented as $c_i = \rho_i \times x_i$. Mineral dissolution occurs rapidly near the injection wells, leading to a rapid increase in pore structure connectivity. Calcite can quickly dissolve in acid in the form of separating particles and biogenic debris fragments, causing changes in the pore network (Lamy-Chappuis et al., 2014). The resulting enhancement in pore connectivity—particularly when dissolution is localized at constricted pore throats—can significantly increase permeability (Dai et al., 2020b). In our study, we assume that only dissolution reactions take place within the simulation domain and salt precipitation processes are neglected. The corresponding evolution of permeability and porosity is described by the following relationship (Saaltink et al., 2013b):

$$\phi = \phi_0 + x_{CaCO_3} \left(\frac{c_{CaCO_3,r}}{c_{CaCO_3,0}} \right), \quad (9a)$$

$$k = k_0 \left(\frac{\phi}{\phi_0} \right)^3 \left(\frac{1-\phi_0}{1-\phi} \right)^2, \quad (9b)$$



where x_{CaCO_3} and c_{CaCO_3} represents the mass fraction and concentration of calcite, subscript 0 and r represent the initial state and
135 the quantity involved in the reaction.

2.3 Gravity-induced ripening

Residual trapped bubbles undergo mass transfer toward the top of the reservoir via Ostwald ripening under the influence of gravity.
The timescale for the system to reach thermodynamic equilibrium through ripening in a 50-meter-thick formation can extend to
several tens of thousands of years—approximately two to three orders of magnitude longer than that of density-driven convection.

140 The following assumptions are introduced in the analysis of the long-term Ostwald ripening process:

(1) After 500 years, the gas distribution stabilizes and attains the initial ripening state, under the assumption that the maximum
dissolution saturation has been achieved throughout the domain.

(2) All bubbles are considered to be in a residually trapped state, with no connectivity between gas phases.

(3) With $dx = 10$ m and $dz = 0.5$ m as the grid size, the gas in the horizontal direction has reached capillary equilibrium, and no
145 mass transfer occurs in the horizontal direction during the following mass transfer process.

The governing equations and simulations used in the ripening process employ the approach presented by Xu et al. (2019a). The
governing equation can be expressed as:

$$\frac{dS_n}{dt} = K_d \frac{d}{dz} \left(C \frac{dP_b}{dz} \right), P_b = P_0 + P_c - (\rho_w - \rho_n)gz, \quad (10)$$

where the gas phase saturation S_n is defined as the bubble volume within the given interval dz relative to the local pore volume. The
150 pore occupancy ratio C refers to the proportion of adjacent pores which are occupied by bubbles. The parameter K_d ($K_d =$
 $n_0 \frac{A_t L_{pore}^2}{2V_{pore} L_t} \frac{V_{mb} D_c}{V_{mw} K^H}$) is a constant related to the pore structure and fluid properties. n_0 is the number of connected pores around a
pore, L_{pore} is the distance between the geometric centers of the adjacent pores, and V_{pore} represents the pore volume. V_{mb} and V_{mw}
represent the molar volumes of the gas and liquid phases, respectively. In the fluid-related component and K^H is the modified
Henry's coefficient. For parameters and detailed procedures related to gravity-induced ripening, please refer to Chen et al. (2022).

2.4 Numerical solution

Due to the strong nonlinearity inherent in the density-dependent flow equations, a fully coupled approach is employed for the fluid
flow and mass transport governing equations. The resulting system of discrete nonlinear equations is solved using the Newton-
Raphson method. Simulations of solute transport and multiphase flow processes are conducted using the finite element software
OpenGeoSys (OGS), version 5. Geochemical reactions are handled by a dedicated Python-based module, OGS-Chem. An interface
160 module has been implemented within OGS to exchange data on CO_2 and calcite concentrations with OGS-Chem (Chen et al., 2020).
Porosity is updated at each time step through the variation of the volume fraction of individual minerals, while permeability is
modified by applying equation (9b).

A script was used to extract the final longitudinal saturation and permeability distributions from the flow and transport simulation,
which then served as the initial conditions for the Ostwald ripening analysis in MATLAB. The ripening simulation models vertical
165 (z-direction) mass transfer only, treating each horizontal column of the grid as a separate, independent 1D simulation.



2.5 Model validation

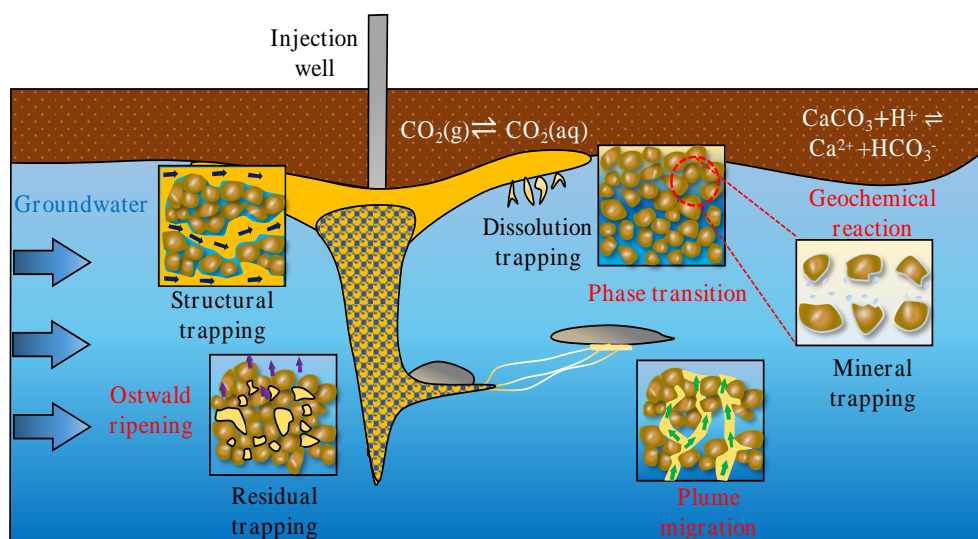
During the injection period, the numerical model was validated through comparison with the semi-analytical solution derived from the theoretical model of Mathias et al (2011). Simulation results demonstrated good agreement with this semi-analytical solution. To further assess the model's performance, a convective mixing scenario was also considered for verification. Due to its sensitivity to mesh discretization (Pau et al., 2010), the results obtained from the model only exhibit similar finger flow patterns and migration distances to the fig.3 of Elenius et al., (2015). Details of injection and dissolution modules validation can be found in our previous research (Chen et al., 2024).

2.6 Grid convergences

Due to the contradiction between the simulation of the field scale and the fine-scale requirement of dissolved CO₂ flow, there is a conflict in grid discretization. The grid size also determines the difficulty of model convergence. Different grid sizes (δx , $\delta z = 0.8, 1, 2, 2.5$) are analyzed in turn, and the average dimensionless concentration ($c^* = \frac{c}{c_{max}}$) in the domain of dissolved CO₂ is selected as the evaluation index to assess the grid convergence. When the finger flow reaches the bottom boundary (200 years), the difference in dimensionless average concentration c^* within the domain does not exceed 0.01 between $\delta x = 0.8$ and $\delta x = 1$. Therefore, in order to balance computational efficiency and accuracy, a resolution of $\delta x = 1$ was selected in subsequent research (Wang et al., 2022b).

3 Numerical Experiments

The integrated model considers multiple processes, including CO₂ injection, migration, dissolution phase transition, reaction with calcite and subsequent ripening process. A schematic diagram is shown in fig. 1.



185 **Figure 1: Schematic diagram of the life-cycle model involving multiple trapping mechanisms. The figure illustrates the primary physical and chemical processes experienced by CO₂ in this model, including injection, dissolution, reaction, and ripening.**



The simulation domain is configured as a two-dimensional, rectangular saline aquifer under isothermal conditions. Initially, the domain is fully saturated with brine and has a length of L and a thickness of H . The left boundary of the model represents an injection well, injecting at a constant rate r_I for a specified duration T_I and then stops. The top boundary is treated as impermeable to simulate the presence of a low-permeability caprock. Both the right and bottom boundaries are assigned zero concentration gradient conditions. A schematic representation of the model setup is provided in Fig. 2.

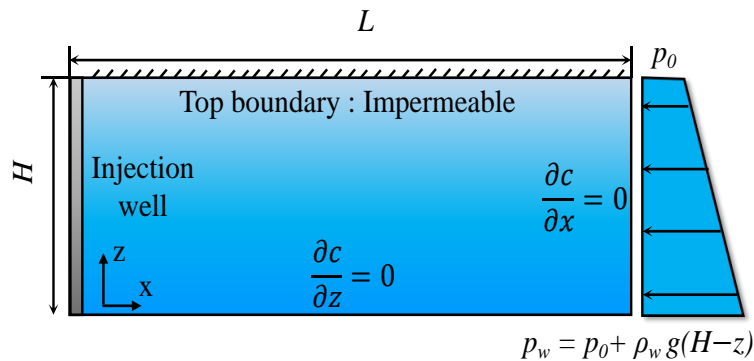


Figure 2: Schematic diagram of 2D numerical model setup with initial and boundary conditions.

Considering the complexity of various physical and chemical processes in the life cycle of GCS, the numerical model that describes the footprint of CO_2 in the formation needs some assumptions. The model proposed in this study mainly includes the following assumptions:

- (1) The entire reservoir is isothermal, and Darcy's law are assumed valid.
- (2) The reservoir is homogeneous, isotropic, and has consistent mineral composition.
- (3) The increase in brine density caused by dissolution is assumed to be linearly related to concentration variations, following the Boussinesq approximation.
- (4) Only calcite, present in the initial mineral composition in the formation, participates in geochemical reactions and its dissolution follows a kinetic rate equation.
- (5) The system is initially saturated with brine and reaches thermodynamic equilibrium, assuming that the brine is in hydro-static state.
- (6) CO_2 is considered pure without water vapor, and the water produced by geochemical reactions is ignored.

Based on the foregoing assumptions, a long-term simulation of the base case was performed. The evolution of the CO_2 plume and pressure distribution, convective mixing dynamics, and reactive transport involving calcite—which induces porosity variations—were systematically examined, with particular emphasis on their mutual interactions. In accordance with the theory of gravity-driven ripening, CO_2 mass transfer was simulated over a period of ten thousand years until the system reached a stabilized state. Sensitivity analyses were carried out to evaluate the influence of calcite content and formation heterogeneity. Two sets of numerical experiments were designed: one examining the long-term evolution of the CO_2 plume and dissolved CO_2 under calcite contents of 0%, 10%, and 20%; the other assessing the effect of heterogeneity coefficients $\gamma = 0.5, 2, \text{ and } 10$.



4 Results and discussion

4.1 CO₂ migration and phase transition

215 Based on the numerical results, saturation-time curves were extracted for monitoring points located along the top boundary of the
reservoir at $x = 20, 40, 60, 80, 100,$ and 120 m, as illustrated in fig.3. During the injection period, the CO₂ plume migrates rapidly
upward, causing a sharp increase in saturation at all monitored locations. Points in close proximity to the injection well continue to
exhibit a brief saturation increase even after injection ceases, attributable to post-injection buoyancy-driven redistribution. Near the
base of the reservoir, the CO₂ gradually accumulates beneath the caprock, with the maximum saturation at any location not exceeding
220 0.45.

After cessation of injection, the plume spreads laterally beneath the caprock and gradually dissolves into the brine. As density-
driven convection intensifies, the dissolution rate increases, leading to a progressive retreat of the plume's leading edge. This
retraction signifies that dissolution limits the lateral extent of the CO₂ plume, thereby enhancing the security of the storage complex.
This behavior is supported by the saturation evolution observed at $x = 100$ m and $x = 120$ m over several hundred years after
225 injection.

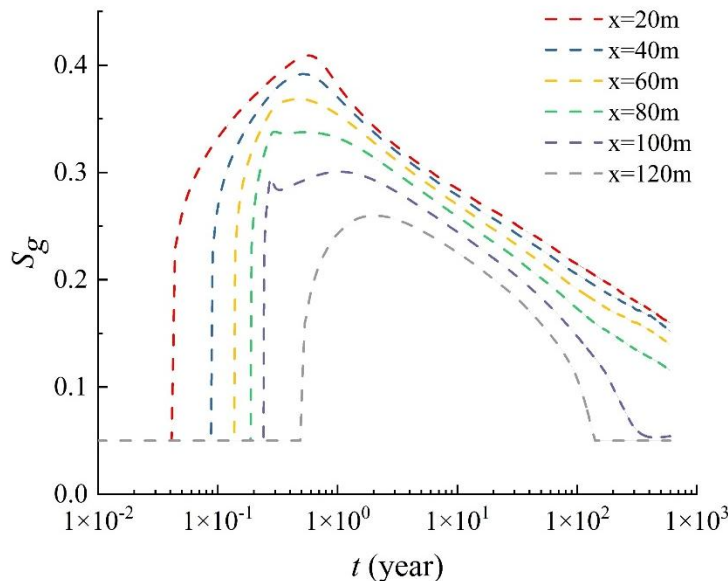


Figure 3: The saturation results of CO₂ for points spaced at 20-meter intervals between 20 and 120 meters throughout the entire simulation period.

Figure 4 illustrates the evolution of the CO₂ plume following the cessation of injection. The plume exhibits a classical funnel-shaped
230 morphology. Within 100 days, buoyancy drives the lower portion of the plume upward to the base of the caprock. The horizontal
migration velocity of CO₂ decreases markedly due to the rapid dissipation of injection-induced pressure.

After 10 years (fig. 4c), the leading edge of the plume has advanced approximately 165 m from the injection well. The overall plume
thickness is significantly reduced, with the maximum thickness decreasing from 10 m to about 5 m. As dissolution continues,



physically trapped CO₂ is progressively converted into the dissolved phase. By 50 years, the plume front has retreated to within 150 m of the well, with a maximum thickness below 5 m and a peak saturation degree of less than 0.3 in the domain.

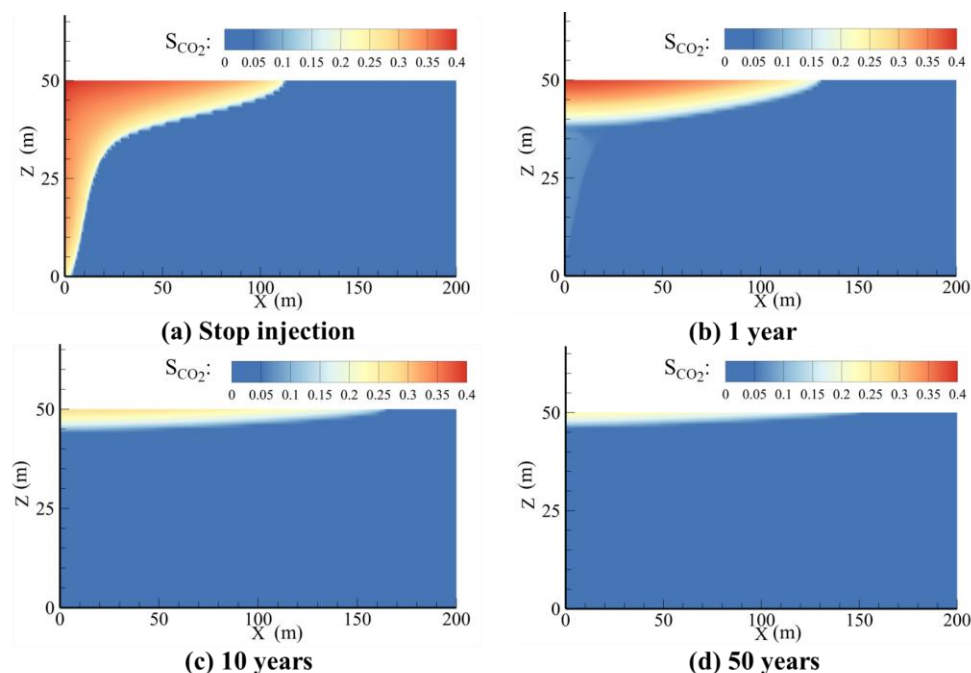
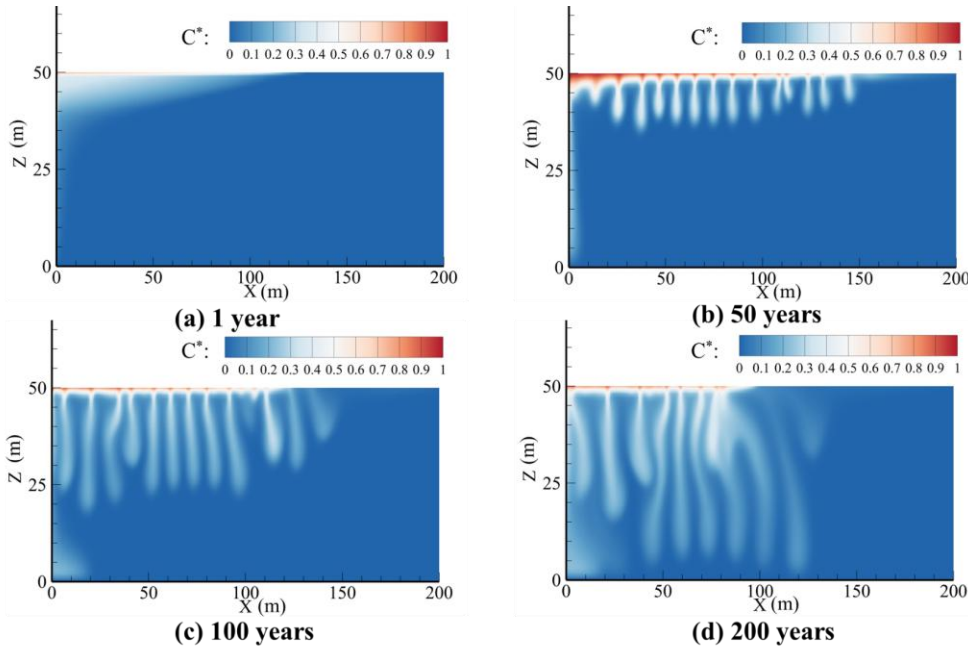


Figure 4: The distribution characteristics of the CO₂ saturations are presented at four key time points: Stopping injection, 1 year after injection, 10 years after injection, and 50 years after injection. After 50 years of dissolution and chemical reactions, the thickness of the CO₂ plume has decreased from over 10 meters to 5 meters.

Figure 5 illustrates the temporal evolution of dissolved CO₂ following the injection period. After injection ceases, the plume accumulation zone exhibits a relatively uniform dissolution pattern. The region of highest concentration is observed at the top of the reservoir, resulting from the elevated CO₂ saturation in this zone. By 50 years, a high-density fingering flow begins to develop, marking a transition from uniform dissolution to distinct convective fingers. The most rapidly migrating finger forms nearest to the injection well, with its tip approaching the bottom of the reservoir.

Within 100 years, the dissolved CO₂ at the top has spread through the finger flow into the saline aquifer, reaching approximately half the reservoir height. After 200 years, interaction between individual fingers becomes evident: those close to the injection well have entered the shutdown period, causing high-concentration fluid to spread laterally along the bottom boundary, which in turn suppresses the development of subsequent fingers. Fingers located farther from the well begin to merge, significantly increasing their width, with the leading edges advancing toward the reservoir base.



250

Figure 5: The concentration distribution of dissolved CO₂ after 1, 50, 100, and 200 years of injection. After 50 years of dissolution, system instability induces finger flow generation, with fingers reaching the bottom after two hundred years.

Figure 6 illustrates the spatial-temporal evolution of reservoir permeability induced by geochemical reactions. The simulated results indicate that significant alterations are predominantly concentrated at the top of the reservoir. The impact of dissolution reactions becomes markedly evident approximately 100 years after injection. By 200 years, the preferential flow pathways formed by permeability enhancement exhibit a strong spatial correlation with the fingering structures depicted in Figure 6. Under sustained acidic conditions, dissolution of calcite results in a local permeability increase of up to approximately 15%.

255

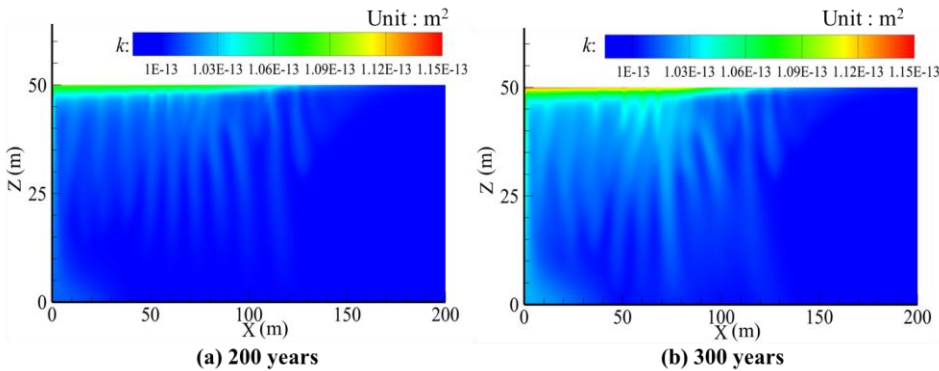


Figure 6: Permeability variations in the reservoir due to geochemical reactions after 200 and 300 years. The dissolution of calcite and the development trend of finger flow are almost overlapping.

260

Figure 7 illustrates the temporal evolution of the contribution of each trapping mechanism in the study case. Given the practical difficulty in distinguishing between structural and residual trapping, these are collectively categorized as physical trapping. The



results indicate that physical trapping remains the dominant mechanism throughout the simulated period, accounting for approximately 80% of total trapped CO₂ during the early injection period (within 100 days). As dissolution and geochemical reactions progress, the proportion of physical trapping gradually decreases to about 60%. The rate of dissolution trapping also slows in the later stages. Mineral trapping constitutes less than 1% of the total, which is consistent with the model setting that only 5% of reservoir calcite is reactive. As dissolved CO₂ concentration declines in later stages, the mineral trapping fraction stabilizes around 0.8%. Although mineral trapping contributes minimally to the total sequestration mass, the enhanced permeability pathways generated by mineral dissolution facilitate the transition of physical trapping to dissolution trapping, thereby improving overall storage security. The long-term effects of geochemical reactions—including changes in chemical composition and pore structure—further investigation under varying reservoir conditions.

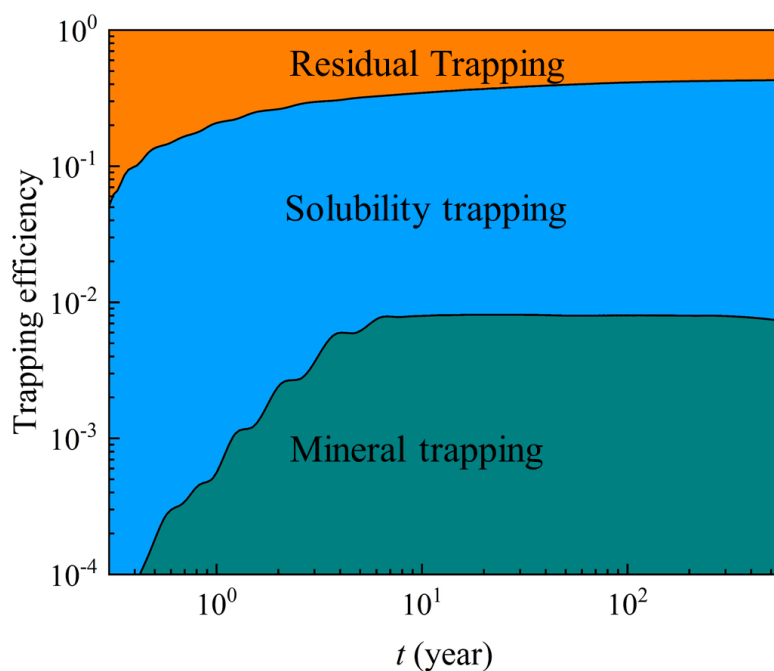


Figure 7: The simulated relative contributions of each trapping mechanisms over time. After 500 years of injection, physical trapping accounts for approximately 60%, dissolved state constitutes about 40%, while mineral trapping remains below 1%.

Figure 8 shows the distribution of CO₂ saturation across the domain at 500 years post-injection. Most of the formation maintains a residual gas saturation close to the minimum value. A thin gas layer persists near the top of the injection well, with a saturation below 0.2 and a thickness of less than 5 meters. Over an extended period of gravity-driven Ostwald ripening, the residual gas undergoes upward mass transfer, accumulating at the top of the reservoir. This process ultimately forms a gas cap approximately 2 meters thick, leaving a bubble-free zone about 45 meters thick at the bottom of the formation. However, the complete mass transfer process spans approximately 80,000 years—two to three orders of magnitude longer than the timescale of the geochemical reactions



considered in this study. As a result, this long-term ripening behavior can only be evaluated through post-processing calculations based on extracted saturation and permeability data from the primary numerical model.

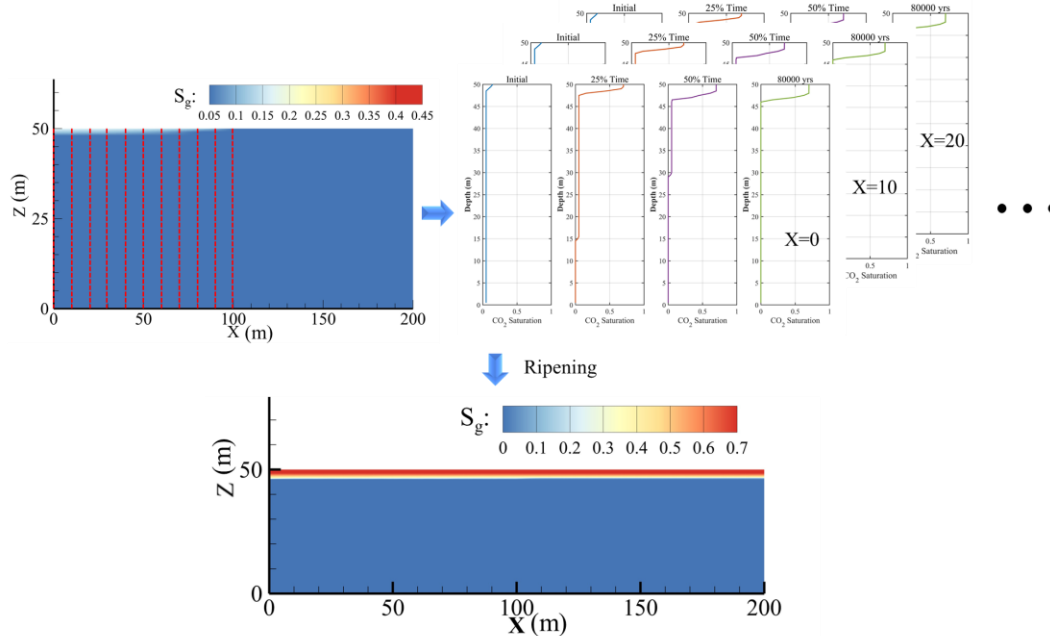


Figure 8: The workflow of data extraction followed by gravity-driven ripening simulations with CO₂ saturation distribution state after 80,000 years. After 80,000 years of secondary distribution, residual trapped CO₂ migrates to the reservoir top under gravity-driven ripening, generating a gas cap at maximum saturation.

4.2 Effect of calcite content

Based on comparative analyses of cases with varying calcite contents (0%, 5%, 10%, and 20%), simulations reveal significant alterations in reservoir porosity after 200 years of geochemical reactions. As illustrated in fig. 9 and 10, the spatial distribution of porosity variation aligns closely with the finger flow pattern across all calcite content scenarios. In the case with an initial calcite content of 20%, the porosity increase near the top of the reservoir reaches approximately 0.01, corresponding to a relative change of about 10%. According to equation (9b), the permeability has increased by approximately 36% relative to the initial value.

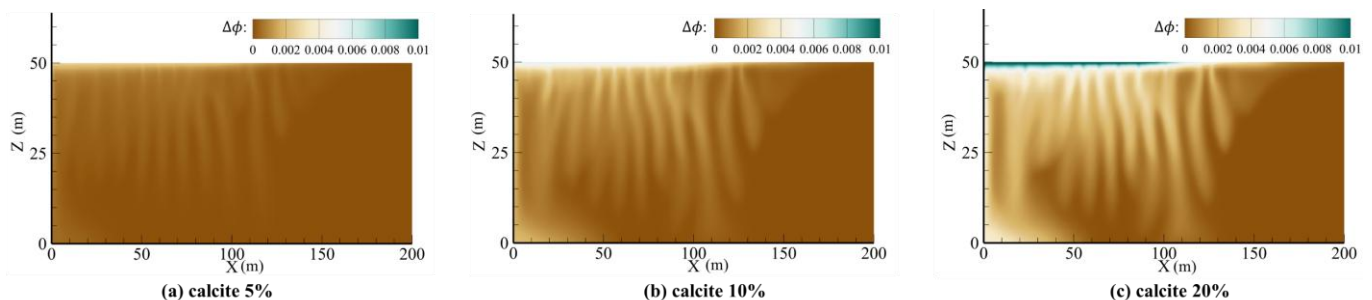


Figure 9: Variations in porosity after 200 years for different calcite content cases. The most intense reservoir dissolution reactions are concentrated at the top of the reservoir.



Figure 10 illustrates the distribution of CO₂ finger flows under different calcite content conditions after three hundred years. As the calcite content increases, a slight increase in the number of fingers is observed, particularly in the 10% and 20% cases. This behavior may be attributed to the formation of localized preferential pathways near the top of the reservoir, which facilitate the development of finger flows along these zones of enhanced permeability. Interestingly, the case with 5% calcite content exhibits the smallest spatial extent of fingering, suggesting that at lower concentrations, the geochemical reactions may inhibit rather than promote the evolution of convective fingers. Overall, the density-driven convective behavior of dissolved CO₂ exhibits low sensitivity to calcite content.

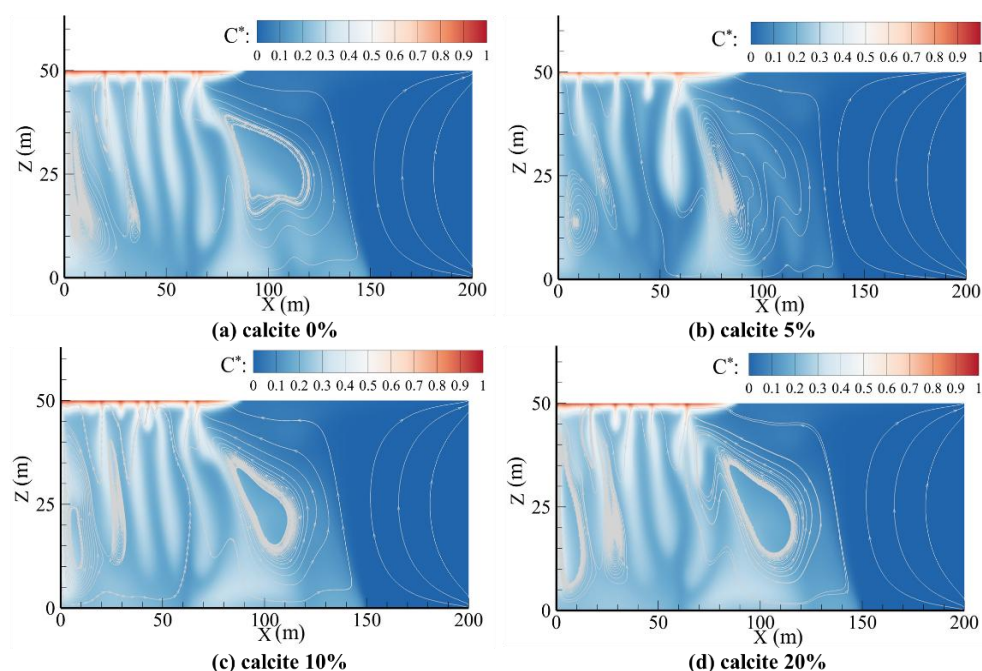


Figure 10: Distribution of dissolved CO₂ concentrations in cases with different calcite contents after 300 years. The case study with 5% calcite content indicates that the presence of dissolution reactions may inhibit the early development of finger flow.

4.3 Effect of heterogeneity

The distribution of the plume in the heterogeneous formation at the time of the cessation of injection is shown in fig.11. A heterogeneity index γ was used to represent the ratio of vertical permeability to horizontal permeability. When $\gamma = 0.5$, the vertical migration of the plume is more efficient, and the injected CO₂ can rapidly accumulate at the top of the reservoir to form a funnel shape with a larger thickness. In contrast, when $\gamma = 10$, the plume exhibits a thinner geometry at the top and migrates laterally over a greater distance. The actual reservoir with smaller vertical permeability is more conducive to the utilization of reservoir space.

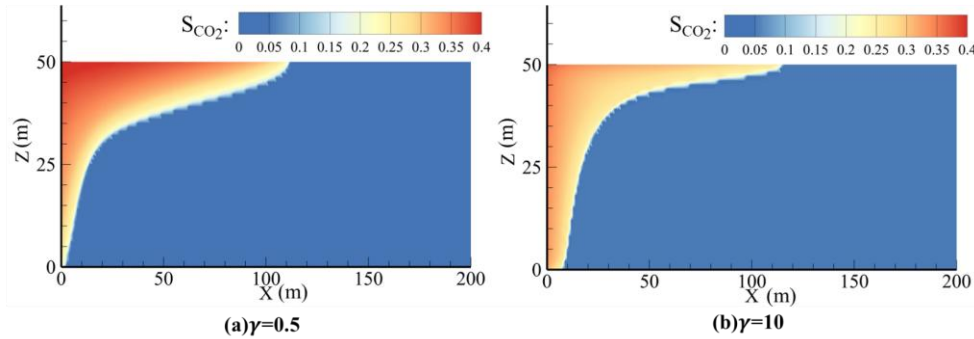


Figure 11: CO₂ plume shape after injection shutdown in heterogeneous formations ($\gamma=1$ and 10).

Figure 12 displays the spatial distribution of CO₂ concentration and flow path characteristics after 200 years with different heterogeneous properties of the formation. It can be observed that as the value of γ increases, it takes longer for the CO₂ in the physically trapped state to be transformed into the dissolved state, which is due to the lower convective strength, and therefore, the finger flow develops more slowly. As shown in fig. 12(a), for $\gamma = 1$, the finger flow has reached the bottom boundary and formed back-flow to inhibit the vertical migration of the top finger flow. There is no strong convective interaction between the finger flows, and the overall vertical development of the finger flows is maintained in case of $\gamma = 2$. When $\gamma = 10$, a high-concentration zone develops at the reservoir top, and fingering flow is largely restricted to the vicinity of the injection well. The resulting fingers exhibit limited vertical development, reaching only about 20 m in height. Under such conditions, the phase transition of physically trapped CO₂ is significantly hindered, which compromises long-term storage security.

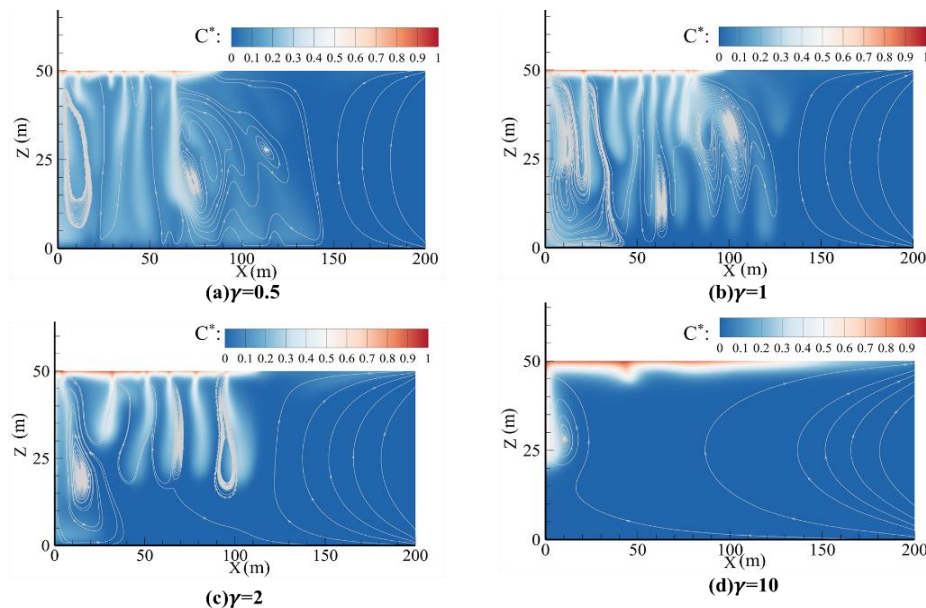


Figure 12: Dissolved CO₂ concentration and flow field distribution state in different formations ($\gamma=0.5, 1, 2$ and 10) after 200 years. The decrease in vertical permeability resulted in delayed development of finger flows and a significant reduction in finger flow numbers.



Figure 13 illustrates the temporal evolution of the average dissolved CO₂ concentration in formations with varying γ . Taking the case of $\gamma = 0.5$ as an example, the rapid increase in the total dissolved storage occurs in two distinct stages. Stage I is governed by the dissolution and phase transition of CO₂, enhanced by the high saturation conditions established during injection. Stage II is characterized by large-scale convective mixing driven by gravitational instability, which significantly augments the dissolution flux.

330 A threefold reduction in the total dissolution amount is observed as γ increases from 0.5 to 10 over the 500-year simulation.

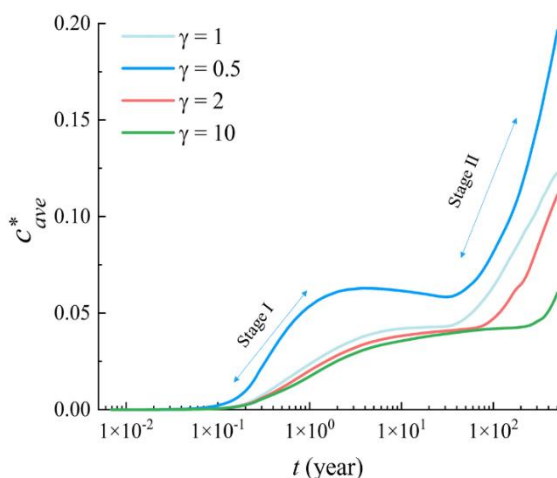


Figure 13: Temporal evolution of the average dimensionless concentration in heterogeneous formations ($\gamma = 0.5, 1, 2$ and 10). The total dissolution amount is divided into two growth stages, exemplified by $\gamma = 0.5$, represented by two-way arrows.

5 Conclusion

335 We have developed an integrated numerical model for geological carbon storage (GCS) that captures the coupling among multiple trapping mechanisms across timescales ranging from days (during CO₂ injection) to millennia (during Ostwald ripening). By incorporating CO₂ injection, dissolution, geochemical reactions, and gravity-driven ripening within a unified framework, the model enables a systematic evaluation of their interactions.

The modeling results and analyses indicate that dissolution trapping reduces the lateral spread of the CO₂ plume by approximately 10% within 50 years. Mineral reactions, though contributing less than 1% to total trapped mass, generate permeability-enhanced pathways that accelerate dissolution. Calcite dissolution promotes the formation of preferential channels that intensify convective fingering, with higher calcite content increasing finger numbers. Geochemical reactions may contribute to a 10% variation in reservoir porosity over 200 years in reservoirs containing 20% calcite. While the migration and mass transfer behaviors of CO₂ are not sensitive to calcite content during the modeling period. Based on the simulation results, vertical permeability anisotropy γ exerts a critical influence on both CO₂ migration and dissolution. Lower γ value significantly enhance vertical migration and dissolution efficiency, whereas higher γ values impede the phase transition of physically trapped CO₂, thereby reducing long-term storage



security. Quantitatively, the total dissolved mass for $\gamma = 0.5$ is approximately three times greater than that for $\gamma = 10$. The proposed model offers a predictive tool for assessing and optimizing long-term GCS security.

Data/Code availability

350 The data that support the findings of this study are available from the corresponding author upon reasonable request.
The numerical model OpenGeoSys version 5 can be downloaded at <https://www.opengeosys.org/releases/#ogs-5>.

Author contributions

RC: Methodology, Validation, Writing - original draft. WX: Conceptualization, Writing - review & editing, Funding acquisition.
YC: Supervision, Funding acquisition. QL: Data curation, Writing - review & editing. TZ: Methodology, Writing - original draft.
355 BG: Visualization, Writing - review & editing.

Competing interests

At least one of the (co-)authors is a member of the editorial board of Hydrology and Earth System Sciences.

Disclaimer

360 Copernicus Publications remains neutral with regard to jurisdictional claims made in the text, published maps, institutional affiliations, or any other geographical representation in this paper. While Copernicus Publications makes every effort to include appropriate place names, the final responsibility lies with the authors. Views expressed in the text are those of the authors and do not necessarily reflect the views of the publisher.

Acknowledgements

365 The authors acknowledge the financial support from research grants provided by the National Natural Science Foundation of China (No. 51988101, 42277128).

References

Bachu, S., Gunter, W. D., & Perkins, E. H. (1994). Aquifer disposal of CO₂: Hydrodynamic and mineral trapping. *Energy Conversion and Management*, 35(4), 269–279. [https://doi.org/10.1016/0196-8904\(94\)90060-4](https://doi.org/10.1016/0196-8904(94)90060-4)



- Bennion, D. B., & Bachu, S. (2008). Drainage and imbibition relative permeability relationships for supercritical CO₂/brine and H₂S/brine systems in intergranular sandstone, carbonate, shale, and anhydrite rocks. *SPE Reservoir Evaluation and Engineering*, 11(3), 487–496. <https://doi.org/10.2118/99326-pa>
- Birkholzer, J. T., Oldenburg, C. M., & Zhou, Q. (2015). CO₂ migration and pressure evolution in deep saline aquifers. *International Journal of Greenhouse Gas Control*, 40, 203–220. <https://doi.org/10.1016/j.ijggc.2015.03.022>
- Carrigan, C. R., Yang, X., LaBrecque, D. J., Larsen, D., Freeman, D., Ramirez, A. L., et al. (2013). Electrical resistance tomographic monitoring of CO₂ movement in deep geologic reservoirs. *International Journal of Greenhouse Gas Control*, 18, 401–408. <https://doi.org/10.1016/j.ijggc.2013.04.016>
- Chen, R., Chen, Y., Xu, W., Hu, Y., Zhan, L., Li, J., et al. (2022). The influence of the hypergravity field during bubble ripening in porous media. *Geophysical Research Letters*, 49(10). <https://doi.org/10.1029/2021GL097005>
- Chen, R., Xu, W., & Chen, Y. (2024). A numerical model for evaluating the long-term migration and phase transition behavior of foam-assisted injection of CO₂ in saline aquifers. *Geoenergy Science and Engineering*, 243(August), 213328. <https://doi.org/10.1016/j.geoen.2024.213328>
- Chen, Y. M., Xu, W. J., Ling, D. S., Zhan, L. T., & Gao, W. (2020). A degradation–consolidation model for the stabilization behavior of landfilled municipal solid waste. *Computers and Geotechnics*, 118(May 2019). <https://doi.org/10.1016/j.compgeo.2019.103341>
- Cui, G., Wang, Y., Rui, Z., Chen, B., & Ren, S. (2018). Assessing the combined influence of fluid–rock interactions on reservoir properties and injectivity during CO₂ storage in saline aquifers. *Energy*, 155, 281–296. <https://doi.org/10.1016/j.energy.2018.05.024>
- Dai, Z., Xu, L., Xiao, T., McPherson, B., Zhang, X., Zheng, L., et al. (2020a). Reactive chemical transport simulations of geologic carbon sequestration: Methods and applications. *Earth-Science Reviews*, 208(January), 103265. <https://doi.org/10.1016/j.earscirev.2020.103265>
- Dai, Z., Xu, L., Xiao, T., McPherson, B., Zhang, X., Zheng, L., et al. (2020b). Reactive chemical transport simulations of geologic carbon sequestration: Methods and applications. *Earth-Science Reviews*, 208(January), 103265. <https://doi.org/10.1016/j.earscirev.2020.103265>
- Dance, T., & Paterson, L. (2016). Observations of carbon dioxide saturation distribution and residual trapping using core analysis and repeat pulsed-neutron logging at the CO₂CRC Otway site. *International Journal of Greenhouse Gas Control*, 47, 210–220. <https://doi.org/10.1016/j.ijggc.2016.01.042>
- Diersch, H. J. G., & Kolditz, O. (2002). Variable-density flow and transport in porous media: Approaches and challenges. *Advances in Water Resources*, 25(8–12), 899–944. [https://doi.org/10.1016/S0309-1708\(02\)00063-5](https://doi.org/10.1016/S0309-1708(02)00063-5)
- Elenius, M. T., Voskov, D. V., & Tchelepi, H. A. (2015a). Interactions between gravity currents and convective dissolution. *Advances in Water Resources*, 83, 77–88. <https://doi.org/10.1016/j.advwatres.2015.05.006>
- Elenius, M. T., Voskov, D. V., & Tchelepi, H. A. (2015b). Interactions between gravity currents and convective dissolution. *Advances in Water Resources*, 83, 77–88. <https://doi.org/10.1016/j.advwatres.2015.05.006>



Elenius, Maria T., Nordbotten, J. M., & Kalisch, H. (2014). Convective mixing influenced by the capillary transition zone. *Computational Geosciences*, 18(3–4), 417–431. <https://doi.org/10.1007/s10596-014-9415-1>

405 Emami-Meybodi, H., & Hassanzadeh, H. (2015). Two-phase convective mixing under a buoyant plume of CO₂ in deep saline aquifers. *Advances in Water Resources*, 76, 55–71. <https://doi.org/10.1016/j.advwatres.2014.11.011>

Emami-Meybodi, H., Hassanzadeh, H., Green, C. P., & Ennis-King, J. (2015). Convective dissolution of CO₂ in saline aquifers: Progress in modeling and experiments. *International Journal of Greenhouse Gas Control*, 40, 238–266. <https://doi.org/10.1016/j.ijggc.2015.04.003>

410 Ennis-King, J., & Paterson, L. (2005). Role of convective mixing in the long-term storage of carbon dioxide in deep saline formations. *SPE Journal*, 10(3), 349–356. <https://doi.org/10.2118/84344-PA>

Fu, X., Cueto-Felgueroso, L., Bolster, D., & Juanes, R. (2015). Rock dissolution patterns and geochemical shutdown of CO₂-brine-carbonate reactions during convective mixing in porous media. *Journal of Fluid Mechanics*, 764, 296–315. <https://doi.org/10.1017/jfm.2014.647>

415 Guo, R., Sun, H., Zhao, Q., Li, Z., Liu, Y., & Chen, C. (2021). A novel experimental study on density-driven instability and convective dissolution in porous media. *Geophysical Research Letters*, 48(23), 1–10. <https://doi.org/10.1029/2021GL095619>

Györe, D., Gilfillan, S. M. V., & Stuart, F. M. (2017). Tracking the interaction between injected CO₂ and reservoir fluids using noble gas isotopes in an analogue of large-scale carbon capture and storage. *Applied Geochemistry*, 78, 116–128. <https://doi.org/10.1016/j.apgeochem.2016.12.012>

420 Iglauer, S., Wüiling, W., Pentland, C. H., Al-Mansoori, S. K., & Blunt, M. J. (2011). Capillary-trapping capacity of sandstones and sandpacks. *SPE Journal*, 16(4), 778–783. <https://doi.org/10.2118/120960-PA>

Jackson, S. J., & Krevor, S. (2020). Small-scale capillary heterogeneity linked to rapid plume migration during CO₂ storage. *Geophysical Research Letters*, 47(18). <https://doi.org/10.1029/2020GL088616>

425 Jing, J., Yang, Y., Cheng, J., Ding, Z., Wang, D., & Jing, X. (2023). Analysis of the effect of formation dip angle and injection pressure on the injectivity and migration of CO₂ during storage. *Energy*, 280(June), 128021. <https://doi.org/10.1016/j.energy.2023.128021>

Kolditz, O., Bauer, S., Beyer, C., Böttcher, N., Dietrich, P., Görke, U. J., et al. (2012). A systematic benchmarking approach for geologic CO₂ injection and storage. *Environmental Earth Sciences*, 67(2), 613–632. <https://doi.org/10.1007/s12665-012-1656-5>

430 Krevor, S., de Coninck, H., Gasda, S. E., Ghaleigh, N. S., de Gooyert, V., Hajibeygi, H., et al. (2023). Subsurface carbon dioxide and hydrogen storage for a sustainable energy future. *Nature Reviews Earth & Environment*, 4(2), 102–118. <https://doi.org/10.1038/s43017-022-00376-8>

Lamy-Chappuis, B., Angus, D., Fisher, Q., Grattoni, C., & Yardley, B. W. D. (2014). Rapid porosity and permeability changes of calcareous sandstone due to CO₂-enriched brine injection. *Geophysical Research Letters*, 41(2), 399–406. <https://doi.org/10.1002/2013GL058534>

435 Lane, J., Greig, C., & Garnett, A. (2021). Uncertain storage prospects create a conundrum for carbon capture and storage ambitions. *Nature Climate Change*, 11(11), 925–936. <https://doi.org/10.1038/s41558-021-01175-7>



- Martinez, M. J., & Hesse, M. A. (2016). Two-phase convective CO₂ dissolution in saline aquifers. *Water Resources Research*, 52(1).
<https://doi.org/10.1002/2015WR017085>
- Mathias, S. A., de Miguel, G. J. G. M., Thatcher, K. E., & Zimmerman, R. W. (2011). Pressure Buildup During CO₂ Injection into a Closed Brine Aquifer. *Transport in Porous Media*, 89(3), 383–397. <https://doi.org/10.1007/s11242-011-9776-z>
- 440 Mathias, S. A., Gluyas, J. G., González Martínez de Miguel, G. J., Bryant, S. L., & Wilson, D. (2013). On relative permeability data uncertainty and CO₂ injectivity estimation for brine aquifers. *International Journal of Greenhouse Gas Control*, 12, 200–212.
<https://doi.org/10.1016/j.ijggc.2012.09.017>
- Neufeld, J. A., Hesse, M. A., Riaz, A., Hallworth, M. A., Tchelepi, H. A., & Huppert, H. E. (2010). Convective dissolution of carbon dioxide in saline aquifers. *Geophysical Research Letters*, 37(22), 2–6. <https://doi.org/10.1029/2010GL044728>
- 445 De Paoli, M. (2021). Influence of reservoir properties on the dynamics of a migrating current of carbon dioxide. *Physics of Fluids*, 33(1). <https://doi.org/10.1063/5.0031632>
- Pau, G. S. H., Bell, J. B., Pruess, K., Almgren, A. S., Lijewski, M. J., & Zhang, K. (2010). High-resolution simulation and characterization of density-driven flow in CO₂ storage in saline aquifers. *Advances in Water Resources*, 33(4), 443–455.
<https://doi.org/10.1016/j.advwatres.2010.01.009>
- 450 Pini, R., & Benson, S. M. (2013). Simultaneous determination of capillary pressure and relative permeability curves from core-flooding experiments with various fluid pairs. *Water Resources Research*, 49(6), 3516–3530. <https://doi.org/10.1002/wrcr.20274>
- Ringrose, P. S., Furre, A. K., Gilfillan, S. M. V., Krevor, S., Landroslash, M., Leslie, R., et al. (2021). Storage of Carbon Dioxide in Saline Aquifers: Physicochemical Processes, Key Constraints, and Scale-Up Potential. *Annual Review of Chemical and Biomolecular Engineering*, 12, 471–494. <https://doi.org/10.1146/annurev-chembioeng-093020-091447>
- 455 Saaltink, M. W., Vilarrasa, V., De Gaspari, F., Silva, O., Carrera, J., & Rötting, T. S. (2013a). A method for incorporating equilibrium chemical reactions into multiphase flow models for CO₂ storage. *Advances in Water Resources*, 62, 431–441.
<https://doi.org/10.1016/j.advwatres.2013.09.013>
- Saaltink, M. W., Vilarrasa, V., De Gaspari, F., Silva, O., Carrera, J., & Rötting, T. S. (2013b). A method for incorporating equilibrium chemical reactions into multiphase flow models for CO₂ storage. *Advances in Water Resources*, 62, 431–441.
<https://doi.org/10.1016/j.advwatres.2013.09.013>
- 460 Sabo, M. S., & Beekingham, L. E. (2021). Porosity-permeability evolution during simultaneous mineral dissolution and precipitation. *Water Resources Research*, 57(6), 1–15. <https://doi.org/10.1029/2020WR029072>
- Sainz-Garcia, A., Abarca, E., Nardi, A., Grandia, F., & Oelkers, E. H. (2017a). Convective mixing fingers and chemistry interaction in carbon storage. *International Journal of Greenhouse Gas Control*, 58, 52–61. <https://doi.org/10.1016/j.ijggc.2016.12.005>
- 465 Sainz-Garcia, A., Abarca, E., Nardi, A., Grandia, F., & Oelkers, E. H. (2017b). Convective mixing fingers and chemistry interaction in carbon storage. *International Journal of Greenhouse Gas Control*, 58, 52–61. <https://doi.org/10.1016/j.ijggc.2016.12.005>
- Sathaye, K. J., Hesse, M. A., Cassidy, M., & Stockli, D. F. (2014). Constraints on the magnitude and rate of CO₂ dissolution at Bravo Dome natural gas field. *Proceedings of the National Academy of Sciences of the United States of America*, 111(43), 15332–15337. <https://doi.org/10.1073/pnas.1406076111>



- 470 Seyyedi, M., Giwelli, A., White, C., Esteban, L., Verrall, M., & Clennell, B. (2020). Effects of geochemical reactions on multi-phase flow in porous media during CO₂ injection. *Fuel*, 269(February). <https://doi.org/10.1016/j.fuel.2020.117421>
- De Silva, G. P. D., Ranjith, P. G., & Perera, M. S. A. (2015). Geochemical aspects of CO₂ sequestration in deep saline aquifers: A review. *Fuel*, 155, 128–143. <https://doi.org/10.1016/j.fuel.2015.03.045>
- Singh, M., Chaudhuri, A., Chu, S. P., Stauffer, P. H., & Pawar, R. J. (2019). Analysis of evolving capillary transition, gravitational
475 fingering, and dissolution trapping of CO₂ in deep saline aquifers during continuous injection of supercritical CO₂. *International Journal of Greenhouse Gas Control*, 82(February), 281–297. <https://doi.org/10.1016/j.ijggc.2019.01.014>
- Wang, Y., Vuik, C., & Hajibeygi, H. (2022a). Analysis of hydrodynamic trapping interactions during full-cycle injection and migration of CO₂ in deep saline aquifers. *Advances in Water Resources*, 159(July 2021), 104073. <https://doi.org/10.1016/j.advwatres.2021.104073>
- 480 Wang, Y., Vuik, C., & Hajibeygi, H. (2022b). Analysis of hydrodynamic trapping interactions during full-cycle injection and migration of CO₂ in deep saline aquifers. *Advances in Water Resources*, 159(July 2021), 104073. <https://doi.org/10.1016/j.advwatres.2021.104073>
- Wei, Y. M., Kang, J. N., Liu, L. C., Li, Q., Wang, P. T., Hou, J. J., et al. (2021). A proposed global layout of carbon capture and storage in line with a 2 °C climate target. *Nature Climate Change*, 11(2), 112–118. <https://doi.org/10.1038/s41558-020-00960-0>
- 485 Xu, K., Mehmani, Y., Shang, L., & Xiong, Q. (2019a). Gravity-Induced Bubble Ripening in Porous Media and Its Impact on Capillary Trapping Stability. *Geophysical Research Letters*, 46(23), 13804–13813. <https://doi.org/10.1029/2019GL085175>
- Xu, T., Spycher, N., Sonnenthal, E., Zhang, G., Zheng, L., & Pruess, K. (2011). Toughreact version 2.0: A simulator for subsurface reactive transport under non-isothermal multiphase flow conditions. *Computers and Geosciences*, 37(6), 763–774. <https://doi.org/10.1016/j.cageo.2010.10.007>
- 490 Xu, T., Zhu, H., Feng, G., Yang, Z., & Tian, H. (2019b). Numerical simulation of calcite vein formation and its impact on caprock sealing efficiency – Case study of a natural CO₂ reservoir. *International Journal of Greenhouse Gas Control*, 83(January), 29–42. <https://doi.org/10.1016/j.ijggc.2019.01.021>
- Zhou, Q., Yang, X., Zhang, R., Hosseini, S. A., Ajo-Franklin, J. B., Freifeld, B. M., et al. (2020). Dynamic Processes of CO₂ Storage in the Field: 1. Multiscale and Multipath Channeling of CO₂ Flow in the Hierarchical Fluvial Reservoir at Cranfield, Mississippi.
495 *Water Resources Research*, 56(2), 1–30. <https://doi.org/10.1029/2019WR025688>